PCCP

RSC Publishing

PAPER

View Article Online
View Journal | View Issue

Cite this: *Phys. Chem. Chem. Phys.*, 2013, **15**, 2125

Pd nanocrystals on WC as a synergistic electrocatalyst for hydrogen oxidation reactions†

Hee-Young Park,[ab] In-Su Park,[a] Baeck Choi,[a] Kug-Seung Lee,[a] Tae-Yeol Jeon,[a] Yung-Eun Sung*[a] and Sung Jong Yoo*[b]

Received 17th September 2012,
Accepted 3rd December 2012

DOI: 10.1039/c2cp43262e

www.rsc.org/pccp

Electrocatalysts for hydrogen oxidation reactions (HORs) are the key to renewable-energy technologies including fuel cells, hydrogen pumps, and water splitting. Despite the significant technological interest and tremendous efforts that have been made, development of hydrogen electrode catalysts with high activity at low cost remains a great challenge. Here, we report the preparation, characterization, and electrochemical properties of a hybrid material composed of Pd nanocrystals grown on spontaneously oxidized WC as a high-performance catalyst for the HOR. The Pd/WC hybrid exhibits enhanced catalytic activity compared to a carbon supported Pd (Pd/C) catalyst, making it a Pt-free, effective catalyst for the HOR. The remarkable catalytic activity arises from synergistic ligand effects between Pd and WC.

1. Introduction

The hydrogen oxidation reaction (HOR) is of central importance in electrochemistry and plays a pivotal role in energy conversion devices, which lead to reduction in our reliance on environmentally unfriendly fossil fuels.[1,2] Pt and its alloys remain the most efficient HOR catalysts, but the high cost and scarcity of Pt hamper further development of fuel cell technologies based on these materials. In this respect, a broad range of alternative catalysts based on precious metals (Rh, Pd, Ir, *etc.*), nitrogen-coordinated metals on carbon, and metal-free doped carbon materials have been actively pursued.[3–11] Metal catalysts frequently suffer from dissolution, sintering, and agglomeration during operation of the fuel cell, which can result in catalyst degradation.[12] To overcome this obstacle, nanostructured catalyst supports such as carbon (active carbon, porous carbon, carbon nanotubes, and graphene), carbide, mesoporous silica, and conducting polymers have been developed to maximize the electroactive surface areas of catalysts and improve their catalytic activity and durability.[12] Among these, WC, which has bulk electronic properties similar to those of Pt-group metals,[13] has emerged as a new-generation catalyst support because of its excellent electrical conductivity, good chemical and environmental stability, CO tolerance, and ability to help increase the dispersion of precious metals.[14] Despite the significant technological interest in carbide-supported precious metal catalysts for the electrocatalytic reaction, there have been no reports of the controllable assembly of Pd nanoparticles supported on WC networks as HOR catalysts. Such systems are attractive targets as they would allow the utilization of the unique features of WC, such as the metal–support interaction.

In this paper, we discuss the preparation, characterization, and electrochemical properties of Pd/WC, a novel class of HOR catalysts in which monolithic Pd NPs are supported on spontaneously oxidized WC. These WC hybrids show an interconnected framework of Pd with uniform deposition of Pd NPs. In the course of our studies on the effects of the WC support on the Pd nanocatalyst, we found that the Pd/WC catalysts exhibit higher exchange current density, lower adsorption energy of atomic hydrogen on the Pd surface, and lower activation energy for the HOR in acid media compared to Pd NPs supported on carbon black.

2. Experimental

2.1 Catalyst preparation

$Pd(NO_3)_2$ (Aldrich, 99.9%), $NaBH_4$ (Aldrich, ACS reagent grade), WC (Alfa Aesar, nanopowder), Vulcan® XC72 (Cabot Corp.), H_2SO_4 (Aldrich, ACS reagent grade), and 2-propanol (Aldrich, HPLC grade) were used without further purification. All solutions were prepared using Milli-Q water (18.3 Ω).

[a] *World Class University (WCU) Program of Chemical Convergence for Energy & Environment (C2E2), School of Chemical & Biological Engineering, Seoul National University, Seoul 151-744, Republic of Korea. E-mail: ysung@snu.ac.kr; Fax: +82 2 888 1604; Tel: +82 2 880 1889*

[b] *Fuel Cell Research Center, Korea Institute of Science and Technology, 39-1 Hawolgok-dong, Seoul 136-791, Republic of Korea. E-mail: ysj@kist.re.kr; Fax: +82 2 958 5199; Tel: +82 2 958 5260*

† Electronic supplementary information (ESI) available: XPS data table, HOR current density, and Arrhenius plot. See DOI: 10.1039/c2cp43262e

For the 1 wt% Pd/WC catalyst, WC powder (1.8615 g) was dispersed in water (800 mL) with ultrasonic treatment and stirring. An aqueous solution of $Pd(NO_3)_2$ (0.0479 g) was added and the solution was stirred to ensure complete mixing. After 12 h, the reduction process was conducted using an aqueous solution (20 mL) of $NaBH_4$ (0.0684 g). The product was filtered and washed with water, then dried at room temperature. The 20 wt% Pd/C was prepared by the same procedure using Vulcan® XC72R in place of WC powder. The Pd/WC catalyst was subjected to three different thermal treatment conditions (200 °C, 400 °C, and 600 °C) under H_2 to investigate the effect of post-treatment.

2.2 Characterization

2.2.1 Physicochemical analysis. Transmission electron microscopy (TEM) images of the Pd/WC and Pd/C catalysts were taken using a JEOL JEM-2010 TEM with an applied voltage of 100 kV. Images were taken of finely ground catalysts that were dispersed in ethanol using an ultrasonic bath and then dropped onto a carbon-coated copper grid. The grid was dried at 70 °C under vacuum for 12 h.

A Rigaku D/max-2500 diffractometer operated with a Cu Kα source (λ = 1.541 Å) at 40 kV and 200 mA was used for powder X-ray diffraction (XRD) analysis of the catalysts. The scanning rate was 4 min^{-1} with an angular resolution of 0.05° for the 2θ scan. X-ray photoelectron spectroscopy (XPS) analysis was conducted with an AXIS-His (Kratos). The binding energies of Pd and W were calibrated with respect to the C 1s level. The XPS spectra were curve-fitted using XPSPEAK 4.1 software. X-ray absorption spectroscopy (XAS) analysis was conducted at the 7C1 beam line at the Pohang Acceleration Laboratory (PAL). The PAL storage ring was operated at an electron energy of 2.5 GeV and an electron current of 150–170 mA. Monochromatic X-ray analysis was conducted using a Si(111) double crystal monochromator and detuned by 30% to minimize contamination from higher harmonics. Before measurement, X-ray energy was calibrated by measuring XAS spectra of Pd or W foil. XAS signals were analyzed using ATHENA software to produce normalized X-ray absorption near edge spectra (XANES).[15]

2.2.1 Electrochemical measurements. An Autolab PGSTAT20 potentiostat (Metrohm Autolab B.V.) was used in all electrochemical measurements. The experiments were conducted in a standard three-compartment electrochemical cell with temperature control and a rotating disk electrode (RDE) system (Eco Chemie B.V.). A saturated calomel electrode (SCE) and a glassy carbon (GC) electrode were used as the reference and counter electrodes, respectively. However, all potentials were calibrated using a homemade reversible hydrogen electrode (RHE) and reported with respect to the RHE. A catalyst-coated GC electrode (5 mm in diameter) was used as the working electrode. The GC electrode was successively polished with slurries of 1 μm, 0.3 μm, and 0.05 μm Al_2O_3 (Buehler) and washed ultrasonically with water before every use. Ink slurry was prepared by mixing Pd/WC or Pd/C catalysts, 5 wt% Nafion® solution (Aldrich), and 2-propanol. The amount of the ink slurry (35 μg cm^{-2} of Pd on the working electrode) was carefully controlled and deposited on the GC electrode, then dried at 70 °C for 5 min to prevent detachment of the catalysts. The electrolyte (0.5 M H_2SO_4) was prepared with Milli-Q water and concentrated H_2SO_4. To measure the HOR current, chronoamperometry was conducted at 15 mV *vs.* RHE in an H_2-saturated 0.5 M H_2SO_4 solution for 600 s.

The current–voltage profiles of real fuel cells were collected from a fuel cell test system (OneATech) operating at a temperature of 70 °C. The anode electrode was fabricated with 0.04 mg cm^{-2} of Pt or Pd. Commercial 40 wt% Pt/C (Johnson Matthey) was applied to a cathode electrode with 0.4 mg cm^{-2} of Pt. The fuel and oxidant were 150 cm^3 min^{-1} of fully humidified H_2 and 200 cm^3 min^{-1} of a fully humidified O_2–N_2 mixture (2 : 8), respectively.

3. Results and discussion

The Pd/WC hybrid was synthesized in solution using a general two-step method. In the first step, Pd NPs were grown on WC freely suspended in solution by chemical reduction of $Pd(NO)_3$ at room temperature. Controlled growth of Pd on WC particles was achieved by adjusting the sintering temperature, which led to crystallization of Pd, and spontaneous oxidation of the WC surface was signaled by a shift in the XPS peaks of tungsten oxide to form the Pd/WC hybrid.

To verify the synergistic effect and the crystallization of the Pd/WC hybrid nanocatalysts, the as-prepared Pd/WC (Pd/WC-AP) catalyst was thermally treated under H_2 gas; the resultant catalysts are denoted Pd/WC-200, Pd/WC-400, and Pd/WC-600 for reduction temperatures of 200 °C, 400 °C, and 600 °C, respectively. As a control sample, a Pd/C catalyst (Pd/C-200) was prepared and reduced under an H_2 atmosphere. The growth of Pd nanocrystals on WC was confirmed by TEM for both Pd/WC-AP and Pd/WC sintered at 200–600 °C. TEM revealed smaller particles in Pd/WC-AP (approximately 5 nm in size, Fig. 1(a)) than in sintered Pd/WC (approximately 10–15 nm, Fig. 1(b)–(d)); this is attributed to the aggregation force of the Pd NPs, which increased Pd particle size and enhanced the crystallization on the sintered Pd/WC. Moreover, the TEM data also showed that the structure of the Pd NPs on WC changed upon thermal treatment. Pd/WC-AP had spherical or cubo-octahedral Pd particles on WC, in good agreement with previous reports.[24] However, the Pd particles on Pd/WC-200 and Pd/WC-400 were pyramidal in shape with little aggregation, likely because of metal–support interactions between surface oxides of W and Pd.[25,26] Large numbers of aggregated Pd particles were detected for Pd/WC-600 because the reduction temperature of tungsten oxides and the Tammann temperature of Pd and W are *ca.* 600 °C.[27]

Fig. 1(e) shows the XRD patterns of the Pd/WCs thermally treated under H_2 gas. The strong diffraction peaks of WC at 31.6(001), 35.7(100), and 48.4(101) are apparent, but the diffraction peaks of Pd were not detected because of the low concentration of Pd. According to Scherrer equation calculations, the crystalline size of WC was 35 nm for all Pd/WCs.

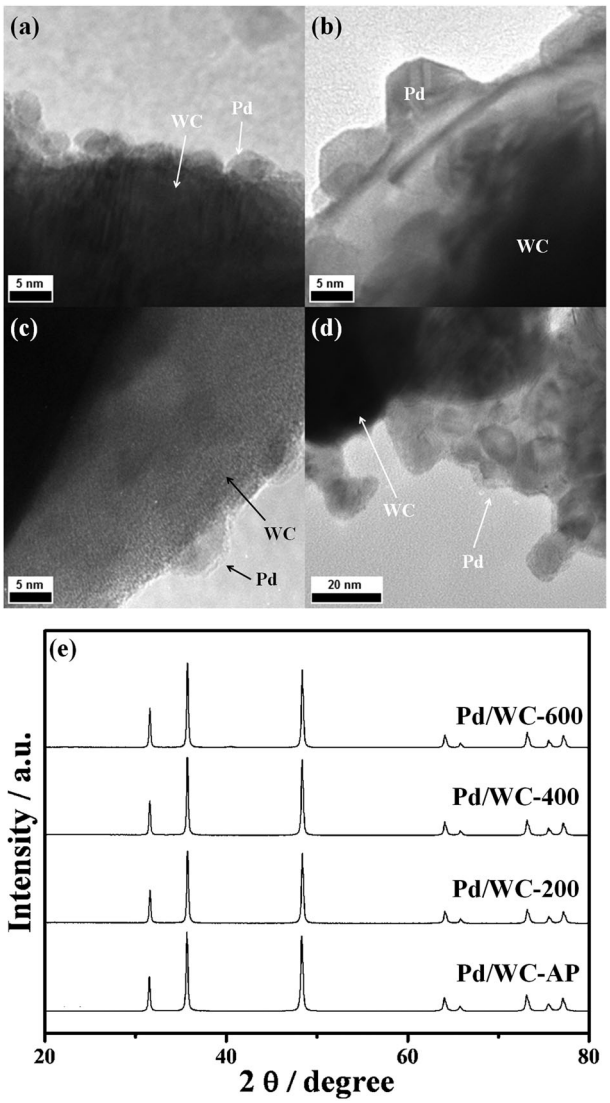

Fig. 1 HR-TEM images of (a) Pd/WC-AP, (b) Pd/WC-200, (c) Pd/WC-400 and (d) Pd/WC-600, (e) XRD patterns of Pd/WC-AP, Pd/WC-200, Pd/WC-400 and Pd/WC-600.

Despite the increase in the reduction temperature, the crystalline structure of the WC was not changed.

To assess their HOR catalytic activity, we characterized HOR polarization on the Pd/C and Pd/WC catalysts in an H_2-saturated 0.1 M H_2SO_4 solution using an RDE. Since Pd has hydrogen absorption/desorption properties near the reversible hydrogen potential, sampled current voltammetry was applied to measure HOR polarization in order to avoid complex overlap between absorbed and bulk hydrogen oxidation (Fig. 2). The electrodes differ with regard to mass-transfer resistance; this resistance should be considered when electrodes have different activity or surface area. Thus, all calculations in our study were conducted using pure kinetic parameters (i_k) from the Koutecky–Levich equation (1).[16]

$$\frac{1}{i} = \frac{1}{i_k} + \frac{1}{i_{l,c}} \quad (1)$$

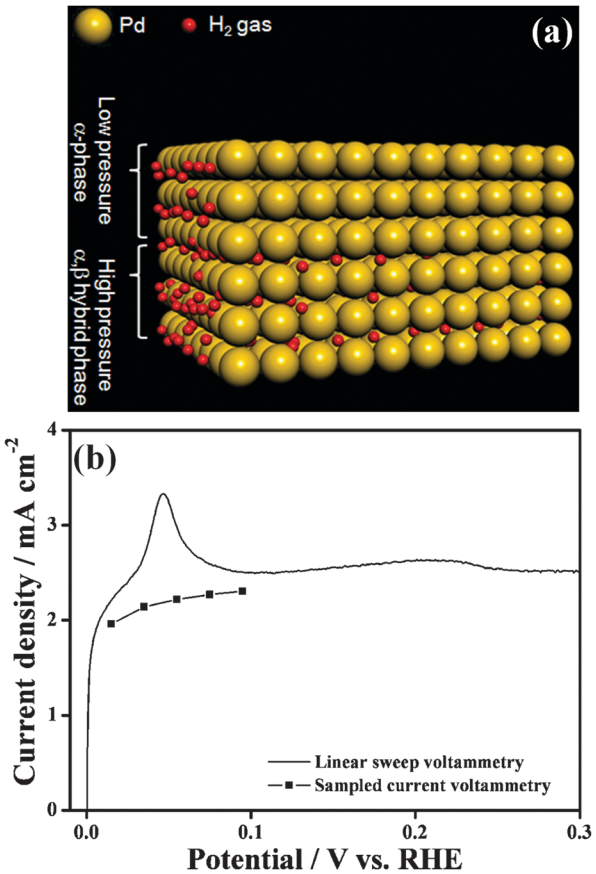

Fig. 2 (a) Schematic model of the Pd metal structure with H atoms in the spaces between the Pd atoms. (b) HOR polarization curves from linear sweep voltammetry (scan rate of 5 mV s^{-1}) and sampled-current voltammetry at the RDE rotation rate of 1500 rpm. The linear sweep voltammograms showed overlap between absorbed and bulk hydrogen oxidation, but sampled-current voltammograms did not.

In eqn (1), i is the measured current, i_k is the kinetic current, and $i_{l,c}$ is the diffusion-limiting current. By measuring i at various values of $i_{l,c}$, the value of i_k, which represents the current in the absence of mass-transfer effects, can be determined. The value of $i_{l,c}$ is given by:

$$i_{l,c} = 0.62nFAD_0^{2/3}\omega^{1/2}\upsilon^{-1/6}C_0^* \quad (2)$$

where n is the number of electrons involved in the reaction (n = 2 for HOR), F is the Faraday constant, A is the electrode area, D_0 is the diffusivity of hydrogen in the electrolyte, ω is the rotating rate, υ is the kinematic viscosity of the electrolyte, and C_0^* is the bulk concentration of hydrogen in the electrolyte. As the diffusion-limiting current depends on $\omega^{1/2}$, plotting i^{-1} *vs.* ω^{-1} allows the determination of i_k^{-1} with four different rotating rates (500 rpm, 1000 rpm, 1500 rpm, and 2000 rpm). Exchange current was calculated using the relation (3) deduced from the Butler–Volmer equation:[16]

$$i = \frac{i_0\eta F}{RT} \quad (3)$$

By plotting the exchange current *vs.* temperatures (2 °C, 6 °C, 10 °C, 14 °C, and 18 °C), it was possible to determine the

apparent enthalpy ($\Delta H^{0\#}$) of the catalyst-mediated reactions by using the Arrhenius equation (4):[17]

$$\frac{\mathrm{d}\log i_0}{\mathrm{d}\left(\frac{1}{T}\right)} = -\frac{\Delta H^{0\#}}{2.3R} \quad (4)$$

where i_0 is the exchange-current density, T is the temperature, and $\Delta H^{0\#}$ is the apparent enthalpy of the reaction. The slope of the linear plot indicates the apparent enthalpy and is presented in Fig. 3(a). The apparent enthalpy represents the activation energy of the reaction on the catalysts and was measured as follows: 66.3 kJ mol^{-1} (Pd/WC-AP), 53.8 kJ mol^{-1} (Pd/WC-200), 40.8 kJ mol^{-1} (Pd/WC-400), and 30.5 kJ mol^{-1} (Pd/WC-600). It might be useful to provide the apparent enthalpy of Pd/C-200 here as well. As shown in Fig. 3(b), the apparent enthalpies decreased when the binding energy (BE) of Pd $3d_{5/2}$ increased. This means that Pd/WC hybrid nanocatalysts with weaker H adsorption energy lead to lower activation barriers for the HOR. In general, for hydrogen dissociation, the strong binding of hydrogen would be thought to imply a low hydrogen activation energy barrier.[22] When hydrogen is adsorbed on a Pt metal surface, the σ (bonding) electrons of hydrogen form a coordinate covalent bond. At the same time, the Pt d-band orbital lobes overlap the empty hydrogen σ^* (antibonding) orbital to form a back-bonding interaction, which strengthens the adsorptive bond between Pt and the head hydrogen atom, weakening the bond between the two hydrogen atoms.

Why, then, is the catalytic behavior of Pd/WC catalysts controversial, as the field of electrochemistry research generally considers the rate-determining step (RDS) of the HOR to be dissociative adsorption of molecular hydrogen?[18,19] It is assumed that electrochemical desorption of protons readily occurs on Pt-group metal surfaces at reversible hydrogen-potential regions. Higher BE thus reduces transition-state energy, and consequently activation-energy barriers. Recently, Rau *et al.* reported that the RDS of HOR on Pd may be desorption of adsorbed hydrogen on α-Pd and β-Pd.[20] Santos and Schmickler also argued that the RDS of the HOR on Pt or Pd, which adsorb atomic hydrogen, may be hydrogen desorption due to a solvation effect.[21] Therefore, the lower apparent enthalpy of the HOR on the Pd/WC catalysts was related to the higher BE by XPS, indicating lower adsorption energy of atomic hydrogen, and can be explained by the latter conclusion of desorption-controlled HOR.

Fig. 4(a) shows an increase in the Pd(0)/Pd_{total} ratio from 27% for Pd/WC-AP to 44%, 49%, and 54% for Pd/WC-200, Pd/WC-400, and Pd/WC-600, respectively. It is possible that native oxides on the Pd particles were removed during thermal treatment and increased the Pd(0)/Pd_{total} ratio in reduced Pd/WCs. The presence of less surface oxides explains the improved activity of reduced Pd/WCs compared to Pd/WC-AP. However, Pd NPs with higher amounts of Pd(0) showed higher BEs, but

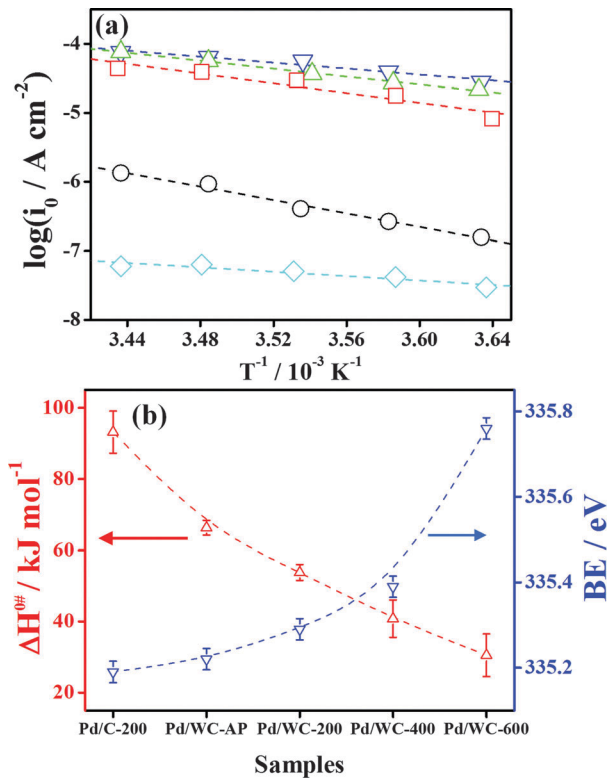

Fig. 3 (a) Arrhenius plots of HOR on Pd/C-200 (○), Pd/WC-AP (□), Pd/WC-200 (△), Pd/WC-400 (▽), and Pd/WC-600 (◊). (b) Binding energies (BEs, blue) of Pd $3d_{5/2}$ and apparent enthalpies (red) of the HOR. These plots were obtained from Fig. S4–S8 (ESI†) and the data of BEs were obtained from XPS of Pd 3d (see Fig. S3 and Table S1, ESI†).

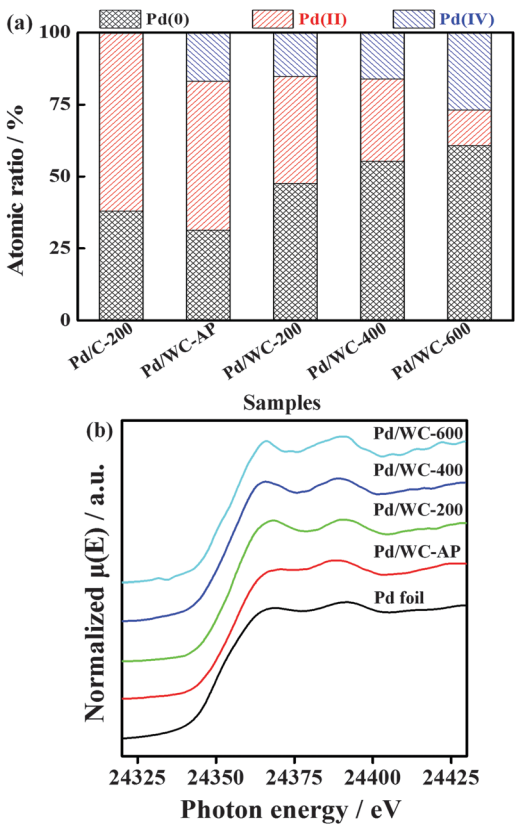

Fig. 4 (a) Area ratios of the Pd 3d regions of the catalysts and (b) XANES of Pd foil, Pd/WC-AP, Pd/WC-200, Pd/WC-400 and Pd/WC-600.

this did not appear to result from reduction of surface oxides. Therefore, we focused on the metal–support interface as a possible reason for the shift of the XPS peak. In order to investigate the influence of metal–support interactions on the XPS-peak shift, XAS analysis was performed at the Pohang Accelerator Laboratory (PAL, 7C1 beam line). The XANES region of the XAS spectrum exhibits a significant increase in the first peaks (the so-called "white line") for Pd/WC-200, Pd/WC-400, and Pd/WC-600 (Fig. 4(b)). One significant aspect of XANES analysis is that it can provide important information about the Pd d-band vacancy. As shown in Fig. 4(b), it corresponds well to the trend of Pd 3d-peak shift in reduced Pd/WCs. However, there was little increase in the white line for Pd/WC-AP. The XANES spectra of the Pd K edge have two significant peaks that correspond to the p and f characters of the density of the final state.[22] Generally, the first peak (the white line) is related to the oxidation state of 4d transition metals or their interactions with their surroundings.[23] Interestingly, Pd/WC-200, Pd/WC-400, and Pd/WC-600 demonstrate larger white lines than Pd/WC-AP, even though the latter had a lower Pd(0) ratio than these reduced Pd/WCs by XPS. If the large increases of the white lines were the result of Pd-particle oxidation, Pd/WC-AP should exhibit a larger white line than the reduced Pd/WCs owing to significant oxidation of Pd particles in Pd/WC-AP and Pd/C by XPS. It can be concluded that the large increase in the white lines in reduced Pd/WCs is not attributable to the oxidation of Pd particles, but may be affected by the metal's surroundings owing to metal–support interface interactions.

The nature of the support surface is one of the most important properties of supported nanoparticles. To characterize the WC surface structure, surface oxide development during the catalyst preparation process was analyzed by XPS, revealing that WC surface oxides dramatically increased after addition of Pd salts (Fig. 5). Therefore, it can be speculated that the Pd precursor acted as an oxidizing agent and Pd particles were deposited on the oxide surface. The effect of the thermal treatment of the Pd/WCs on the WC support was also monitored at various reduction temperatures (Fig. 6). The BEs of W $4f_{7/2}$ shifted considerably from 35.7 eV to 35.5 eV when reduction temperatures were altered from 200 °C to 600 °C. Generally, a negative shift of BE in oxide materials implies an oxygen-deficient state, and electron transfer between the oxide materials and metal may occur with ease if the oxides are in the reduced state. Thus, it can be suggested that electron transfer from Pd to WC is a major contributor to increases in white lines and the positive shift of the Pd 3d XPS core-level peaks in reduced Pd/WCs. Therefore, it is likely that metal–support interactions are a major factor for improved activity in our catalysts.

From a practical standpoint, the mass-specific activity of electrocatalysts is an important issue in reducing costs. Therefore, we additionally measured the efficiency using the current–voltage profile of real fuel-cell systems (Fig. 7). It is well known that lowering Pt loading from 0.4 mg cm^{-2} to 0.05 mg cm^{-2} in anodes evokes a voltage drop of no more than 15 mV at the current density of 1.2 A cm^{-2}.[28] Although there are differences between the electrode structures of carbon- and WC-supported catalysts, electrode mass-transfer resistance is negligible in regions of low current density. Thus, assuming that the fuel cells have identical cathode electrode conditions, it can be assumed that the voltage drops in Pd-catalyzed fuel cells resulted from anodic overpotential. At a current density of 200 mA cm^{-2}, the potential drops of Pd/C, Pd/WC-200, Pd/WC-400, and Pd/WC-600 were 89 mV, 29 mV, 48 mV, and 735 mV, respectively. The most efficient

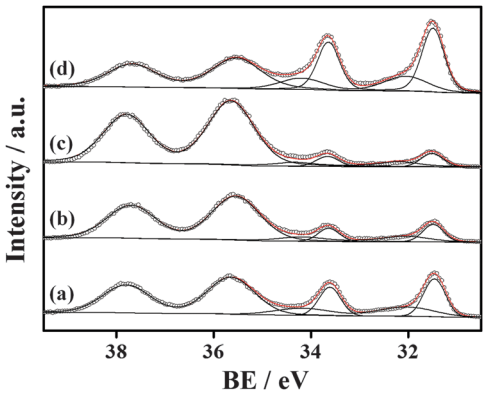

Fig. 6 The W 5f XPS spectra of (a) Pd/WC-AP, (b) Pd/WC-200, (c) Pd/WC-400 and (d) Pd/WC-600.

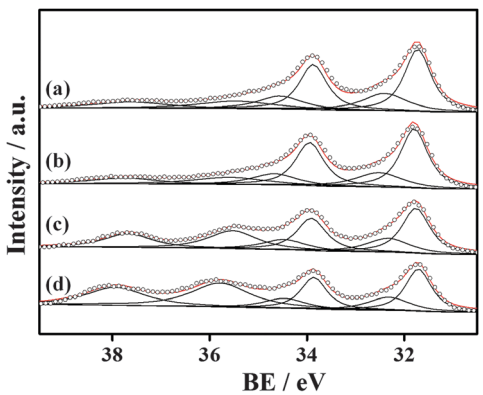

Fig. 5 The W 4f XPS spectra of (a) fresh WC, (b) after mixing with DI water for 12 h, (c) after mixing with Pd salt and stirring for 12 h and (d) Pd/WC-AP.

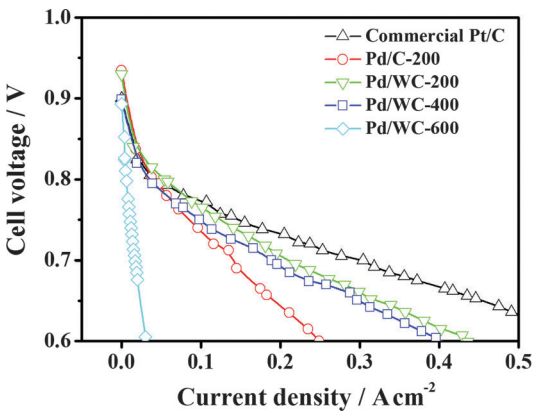

Fig. 7 Current–voltage profiles of fuel cells with anode catalysts of commercial Pt/C, Pd/C-200, Pd/WC-200, Pd/WC-400 and Pd/WC-600.

catalyst was Pd/WC-200, which demonstrated only 1/3 of the potential drop of Pd/C-200. Despite the fact that Pd/WC-600 exhibited the lowest apparent enthalpy, its potential drop was large in a real fuel cell. The specific active areas of the catalysts were not determined because of their instability at regions of high potential, but we suspect that the low mass activity of Pd/WC-600 may originate from a low specific area owing to coalescence of Pd particles.

4. Conclusion

Controlled growth of Pd on WC particles was achieved using a simple two-step procedure at different reduction temperatures to provide Pd/WC catalysts for HOR. Electrochemical studies of the Pd/WC catalysts indicated that weaker H adsorption energy led to lower activation barriers for the HOR. However, the notion that Pd NPs with lower atomic hydrogen adsorption energies should have higher activity is still under debate. Pd absorbs hydrogen, altering its electron structure and this makes theoretical studies of the HOR on hydride-modified Pd surfaces more difficult. From a practical point of view, we have investigated the use of Pd/WC electrocatalysts for proton exchange membrane fuel cells (PEMFCs) and found that Pd/WC-200 was the most efficient catalyst. In addition, we characterized the promoting effect of the WC support. Our studies also raise promising possibilities for investigation of the HOR on hydride-modified Pd surfaces. Continuing research will be necessary in order to clearly interpret oxide enhancement of the HOR on hydride-modified Pd. Our current research suggests the possibility of using Pd/WC hybrid nanocatalysts for practical applications and the fundamental knowledge obtained from our study will be useful in realizing improvements in Pt-free anode catalysts.

Acknowledgements

This research was supported by the National Research Foundation of Korea funded by the Ministry of Education, Science and Technology (NRF-C1AAA001-2010-0029065) and WCU program (R31-10013). This work was also supported by the Global Frontier R&D Program on the Center for Multiscale Energy System funded by the NRF under the MEST, Korea.

Notes and references

1 Handbook of Fuel Cells: Fundamentals, Technology and Applications, ed. W. Vielstich, A. Lamm and H. Gasteiger, Wiley, Chichester, UK, 2003.
2 C. Y. Wang, *Chem. Rev.*, 2004, **104**, 4727–4766.
3 F. Jaouen, E. Proietti, M. Lefevre, R. Chenitz, J. P. Dodelet, G. Wu, H. T. Chung, C. M. Johnston and P. Zelenay, *Energy Environ. Sci.*, 2011, **4**, 114–130.
4 D. S. Su and G. Q. Sun, *Angew. Chem., Int. Ed.*, 2011, **50**, 11570–11572.
5 C. J. Chang, Y. Q. Deng, C. N. Shi, C. K. Chang, F. C. Anson and D. G. Nocera, *Chem. Commun.*, 2000, 1355–1356.
6 R. L. Liu, D. Q. Wu, X. L. Feng and K. Müllen, *Angew. Chem., Int. Ed.*, 2010, **49**, 2565–2569.
7 S. Y. Wang, D. S. Yu, L. M. Dai, D. W. Chang and J. B. Baek, *ACS Nano*, 2011, **5**, 6202–6209.
8 C. J. Chang, Z. H. Loh, C. N. Shi, F. C. Anson and D. G. Nocera, *J. Am. Chem. Soc.*, 2004, **126**, 10013–10020.
9 S. Wang, E. Iyyamperumal, A. Roy, Y. Xue, D. Yu and L. M. Dai, *Angew. Chem., Int. Ed.*, 2011, **50**, 11756–11760.
10 A. Morozan, S. Campidelli, A. Filoramo, B. Jousselme and S. Palacin, *Carbon*, 2011, **49**, 4839–4847.
11 Y. Y. Liang, Y. G. Li, H. L. Wang, J. G. Zhou, J. Wang, T. Regier and H. J. Dai, *Nat. Mater.*, 2011, **10**, 780–786.
12 Y. J. Wang, D. P. Wilkinson and J. J. Zhang, *Chem. Rev.*, 2011, **111**, 7625–7651.
13 R. B. Levy and M. Boudart, *Science*, 1973, **181**, 547–549.
14 D. V. Esposito and J. G. Chen, *Energy Environ. Sci.*, 2011, **4**, 3900–3912.
15 B. Ravel and M. Newville, *J. Synchrotron Radiat.*, 2005, **12**, 537–541.
16 A. J. Bard and L. R. Faulkner, *Electrochemical methods: fundamentals and applications*, John Wiley & Sons, Inc., New York, 2nd edn, 2001.
17 N. M. Markovic, B. N. Grgur and P. N. Ross, *J. Phys. Chem. B*, 1997, **101**, 5405–5413.
18 J. X. Wang, T. E. Springer and R. R. Adzic, *J. Electrochem. Soc.*, 2006, **153**, A1732–A1740.
19 S. Chen and A. Kucernak, *J. Phys. Chem. B*, 2004, **108**, 13984–13994.
20 M. S. Rau, P. M. Quaino, M. R. Gennero de Chialvo and A. C. Chialvo, *Electrochem. Commun.*, 2008, **10**, 208–212.
21 E. Santos and W. Schmickler, *Angew. Chem., Int. Ed.*, 2007, **46**, 8262–8265.
22 J. E. Muller, O. Jepsen, O. K. Andersen and J. W. Wilkins, *Phys. Rev. Lett.*, 1978, **40**, 720–722.
23 W. B. Kim, E. D. Park, C. W. Lee and J. S. Lee, *J. Catal.*, 2003, **218**, 334–347.
24 Y. W. Lee, A. R. Ko, S. B. Han, H. S. Kim, D. Y. Kim, S. J. Kim and K. W. Park, *Chem. Commun.*, 2010, **46**, 9241–9243.
25 C. Bigey, L. Hilaire and G. Maire, *J. Catal.*, 1999, **184**, 406–420.
26 C. Bigey and G. Maire, *J. Catal.*, 2000, **196**, 224–240.
27 H. Knözinger and E. Taglauer, *Spreading and Wetting*, Wiley-VCH Verlag GmbH & Co. KGaA, 2008.
28 H. A. Gasteiger, J. E. Panels and S. G. Yan, *J. Power Sources*, 2004, **127**, 162–171.

